Engineered Science
DOI: https://dx.doi.org/10.30919/es1833

Stealth-Communication Switching via A Resistive Metasurface with Dynamically Reconfigurable Transmission Window

Hao Yang,[1,2] Yongfeng Li,[1,2,*] Lixin Jiang,[1,2] Zhe Qin,[1,2] Lei Wang,[1,2] Jiechu Liu,[1,2] Zhihao Guo,[1,2] Lin Zheng,[1,2] Hongya Chen,[1,2] Wenjie Wang[1,2,*] and Jiafu Wang[1,2]

Abstract

The advancement of stealth technology urgently demands electromagnetic (EM) functional materials that can dynamically adapt to complex operational environments. While reconfigurable metasurfaces have enabled dynamic wavefront manipulation, achieving simultaneous and independent broadband absorption and high-efficiency transmission within a single, actively tunable platform remains a significant challenge. In this paper, we propose a novel actively tunable metasurface that overcomes this limitation by demonstrating dynamic switching between a transparent "communication window" and a reflective "stealth mode" within the same frequency band, while maintaining exceptional out-of-band absorption across two broad bands. The design integrates an upper impedance layer with a resistive-film-loaded Jerusalem cross structure to achieve optimal absorption performance, while simultaneously incorporating PIN diodes into the lower multilayer frequency-selective surface to enable dynamic switching functionality. Experimental results demonstrate exceptional performance: over 90% transmission in the ON state with low insertion loss (<2 dB), and less than 10% transmission in the OFF state within the operational band. Simultaneously, the structure maintains greater than 90% absorption across two broad bands (3.4-6.2 GHz and 9.1-15.2 GHz) in both states. This work provides a paradigm-shifting solution for next-generation intelligent stealth platforms, promising applications in radar systems, communication windows for stealth vehicles, and electromagnetic compatibility.

Keywords: Reconfigurable metasurface; Stealth-communication switching; Frequency-selective surface; Broadband absorption; Electromagnetic regulation.
Received: 07 September 2025; Revised: 15 October 2025; Accepted: 22 October 2025
Article type: Research article.

1. Introduction

The intelligent control of electromagnetic (EM) waves using functional materials has become a pivotal technology for modern radar, communication, and stealth systems.[1,2] In particular, the pursuit of low-observable platforms has driven the development of frequency selective surfaces (FSSs), which provide spatial filtering of EM waves to achieve in-band transmission and out-of-band reflection.[3] However, the inherent high radar cross-section (RCS) of traditional FSSs in the stopband renders them vulnerable to advanced detection systems, severely limiting their application in stealth-critical scenarios.[4]

To mitigate this limitation, the concept of frequency-selective rasorbers (FSRs) was introduced, aiming to combine absorption and transmission functionalities within a single structure.[5,6] By integrating resistive elements or lossy structures with band-pass FSS designs, such rasorbers can achieve significant absorption outside the passband while maintaining transmission within a specific frequency window.[7-10] Nevertheless, conventional FSRs are inherently passive and static—their operational bandwidth and functionality are fixed upon fabrication. This inflexibility is a major drawback in the face of increasingly complex and dynamic electromagnetic operational environments, where the ability to actively switch between a high-transmission "communication mode" and a high-reflection "stealth mode" is highly desirable.[11,12]

[1]*Air Force Engineering University, Department of Basic Sciences, Xi'an, Shaanxi, 710051, China*
[2]*Shaanxi Key Laboratory of Artificially-Structured Functional Materials and Devices, Air Force Engineering University, Xi'an, Shaanxi, 710051, China*
[*]*Email:* liyf217130@126.com (Yongfeng Li), wwjie2005@163.com (Wenjie Wang)

Recent advances in reconfigurable metasurfaces have opened new pathways toward dynamic EM wave manipulation.[13,14] As two-dimensional artificial materials composed of subwavelength unit cells, metasurfaces provide an exceptional platform for integrating active components such as PIN diodes, varactors, or micro-electromechanical systems (MEMS) to achieve real-time control over EM responses.[15,16] Several pioneering studies have demonstrated metasurface-based absorbers or FSSs with switchable operating states.[17-18]

Moreover, there is another method synthesizing a class of 3D FSRs to provide solutions of great two-sided absorptions.[19-22] The FSR can create a lossless resonator in the pass band and a lossy resonator in the absorption band, which means it can provide flexible absorption without increasing insertion loss. Furthermore, the structures with multi-interfinger resonators and nested gaps are proposed to realize multi-wave transmission windows,[23-24] but its engineering application is hindered by its complex design and fabrication. Besides, coded metasurfaces designed by the optimized algorithm also provide more choices and dimensions for the design of low reflection FSS.[25-26]

However, most current designs face a critical performance trade-off: the pursuit of reconfigurability often comes at the expense of bandwidth, efficiency, or angular stability. For instance, many designs exhibit narrow transmission windows, high insertion loss, or limited absorption bandwidth, which significantly restricts their practical deployment in broadband systems requiring robust and adaptable performance.[27] This precisely highlights the core operational dilemma facing modern stealth platforms: the conflicting requirements to evade detection by absorbing or reflecting hostile radar signals, while simultaneously receiving friendly communication transmissions. Current static structure force a compromise between these objectives, creating a critical need for surfaces capable of broadband dynamic electromagnetic reconfiguration to maintain both stealth and connectivity during mission execution.

To overcome the limitations of prior designs, we propose a novel metasurface architecture that fundamentally decouples the control of in-band and out-of-band responses. Our core innovation is a multi-functional design integrating a lossy Jerusalem cross resonator with an actively switched FSS layer, enabling independent optimization of broadband absorption and dynamic in-band switching without performance compromise. This approach effectively breaks the traditional trade-off between reconfigurability and bandwidth. Additionally, we introduce a resistive film to replace the conventional lumped resistor to absorb the electromagnetic wave energy through its unique ohmic loss mechanism. The introduction of the resistive film enables the metamaterial absorber to exhibit effective broadband wave absorption at different angles of incidence due to the ability of the resistive film to distribute the electromagnetic wave energy uniformly.The bottom active layer, with integrated PIN diodes, electronically modulates the surface impedance to achieve seamless transitions between a high-transmission 'communication window' and a total-reflection 'stealth mode' within the operational band. This capability is particularly advantageous for modern radar radomes and stealth vehicles, which require on-demand switching between satellite communication windows and full-stealth operational modes.

The remainder of this paper is structured as follows. Section II details the design methodology, including the operational principle, equivalent circuit model, and the analysis of the individual layers. Section III presents the experimental validation of the fabricated prototype, demonstrating its switching performance and wideband absorption characteristics under various illumination conditions. Finally, Section IV discusses the broader implications of our work, compares its performance with state-of-the-art alternatives, and outlines its potential applications in adaptive stealth platforms and smart electromagnetic environments.

2. Design of the metasurface structure

2.1 Overall architecture and operating principle

According to the design in,[15] a metasurface unit is generally composed of a lossy layer and a lossless FSS. In this paper, the structure proposed such an idea to achieve feature of two-side absorption with intermediate transmission but improved to realize a dynamic switching function, as shown in Fig. 1. The structure proposed in this paper uses such an idea to achieve the feature of two-side absorption with intermediate transmission, as illustrated in Fig. 1.

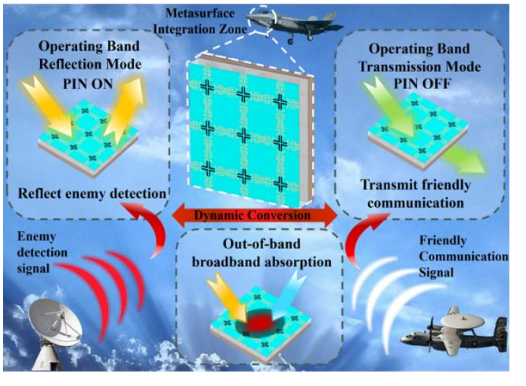

Fig. 1: Functional schematic and operating principle of the proposed structure.

In order to intuitively understand the underlying mechanism, an equivalent circuit model based on transmission line theory is described in Fig. 2. We consider the top lossy layer as a complex impedance Z_A, while the lossless three-layer FSS is regarded as impedance Z_B for better simulation. The dielectric substrate between the two parts can be simulated by a transmission line with length D_1 and characteristic impedance Z_1.

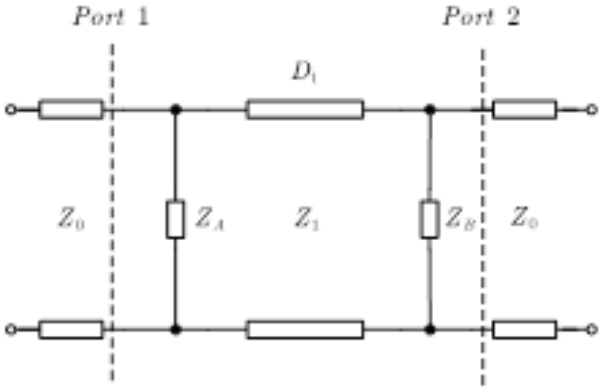

Fig. 2: Transmission line model of the proposed rasorber.

The transmission line model depicted in Fig. 2 can be regarded as a two-port network. According to,[28] the ABCD matrix of the network can be expressed as as Eq. (1):

$$\begin{pmatrix} A & B \\ C & D \end{pmatrix} = \begin{pmatrix} 1 & 0 \\ \frac{1}{Z_A} & 1 \end{pmatrix} \begin{pmatrix} \cos\theta & jZ_1 \sin\theta \\ j\frac{\sin\theta}{Z_1} & \cos\theta \end{pmatrix} \begin{pmatrix} 1 & 0 \\ \frac{1}{Z_B} & 1 \end{pmatrix} = \begin{pmatrix} \cos\theta + j\frac{Z_1}{Z_B}\sin\theta & jZ_1 \sin\theta \\ \frac{Z_A+Z_B}{Z_A Z_B}\cos\theta + j\left(\frac{Z_A Z_B + {Z_1}^2}{Z_A+Z_B}\right)\sin\theta & \cos\theta + j\frac{Z_1}{Z_A}\sin\theta \end{pmatrix} \quad (1)$$

where $\theta=\beta h=2\pi h/\lambda$.

For the feasibility of design, the dielectric interval is filled with foam substrate as general equivalent of air, which means we can assume $Z_1=Z_0$. By making use of the transformation relationship between ABCD matrix and S-parameter matrix, the reflection (S_{11}) and transmission (S_{21}) coefficients of the network can be evaluated.

$$|S_{11}| = \left|\frac{A+\frac{B}{Z_0}-CZ_0-D}{A+\frac{B}{Z_0}+CZ_0+D}\right| = \left|\frac{-Z_0(Z_A+Z_B)\cos\theta + jZ_0(Z_A-Z_B-Z_0)\sin\theta}{[Z_0(Z_A+Z_B)+2Z_A Z_B]\cos\theta + j[Z_0(Z_A+Z_B+Z_0)+2Z_A Z_B]\sin\theta}\right| \quad (2)$$

$$|S_{21}| = \left|\frac{2Z_A Z_B}{A+\frac{B}{Z_0}+CZ_0+D}\right| = \left|\frac{2Z_A Z_B}{[Z_0(Z_A+Z_B)+2Z_A Z_B]\cos\theta + j[Z_0(Z_A+Z_B+Z_0)+2Z_A Z_B]\sin\theta}\right| \quad (3)$$

Under ideal conditions, S-parameters comes into $|S_{11}|=0$ and $|S_{21}|=0$ at the lower absorption band F_L and the upper absorption band F_H. Therefore, we can substitute the above conditions into the two Eqs. (2) and (3) to get the solution of Z_A and Z_B. With ideal performance of rasorber, the numerator in $|S_{11}|$ and $|S_{21}|$ fraction is obviously equal to zero, so relationship between Z_A and Z_B is mentioned in Eqs. (4) and (5):

$$Z_B = \frac{-Z_A \cos\theta + j(Z_A - Z_0)\sin\theta}{\cos\theta + j\sin\theta} \quad (4)$$

$$Z_A Z_B = 0 \quad (5)$$

However, according to the transmission line theory, once $Z_A=0$, the EM wave will be completely reflected in the Z_A layer, and it makes the role of rasorber nonsensical. Therefore, it can be determined that $Z_B=0$.In this case, the expression of Z_A can be deduced as Eq. (6):

$$Z_A = \frac{jZ_0 \sin\theta}{-\cos\theta + j\sin\theta} \quad (6)$$

Therefore, the impedance of the ideal absorber at F_L and F_H are calculated theoretically. In addition, Z_A can have different values because of the domination of θ.[29]

At F_T, both of the absorber and the lossless FSS are transparent for incident waves and thus providing a bandpass with low insertion loss, which means the condition of $|S_{11}|=0$ and $|S_{21}|=1$ can set into Eq. (2)(3). As the impedance of FSS, Z_B is infinite so that the derived formula to determine Z_A is as Eq. (7):

$$\left|\left(\frac{Z_0}{Z_A}+2\right)(\cos\theta + j\sin\theta)\right| = 2 \quad (7)$$

From the above formula, it is clear that ZA is infinite at FT. When the absorber works at FL and FH, its working frequency band generally should meet the requirements of impedance while manifesting as transparent for incident waves in other frequencies. The lossless FSS should not be resistive at FT, and play the same role as which is the same as a metal ground to provide perfect reflection at the absorptive bands.

Accordingly, these conclusion under ideal conditions have certain guiding significance for the design of metasurface, but to make it more in line with the requirements of engineering applications, it is still necessary to optimize its geometric parameters through the combination of numerical simulation and measurement.

The unit cell structure and geometrical details of the proposed structure are shown in Fig. 3. The structure consists of top lossy layer and bottom lossless FSS separated by foams (ε_r=1.05, thickness d=8 mm). The unit sizes of the lossy layer and the lossless FSS are 10mm and 7.5mm respectively, and all the thickness of metal layers is 0.017 mm. The parameters of unit are listed in Table 1.

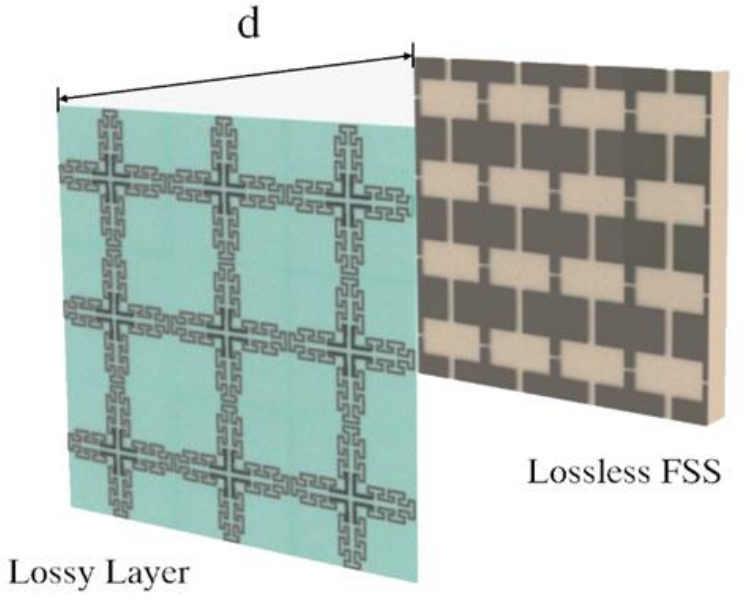

Fig. 3: The geometric configuration of the proposed structure unit cell.

Table 1: The Physical Parameters of Proposed Metasurface Unit.

Parameter	d	d_1	P	p	w_1	w_2	w_3
Value	12	1.575	10	7.5	0.2	0.3	0.3
Parameter	w_4	w_5	w_6	w_7	w_8	l_1	l_2
Value	0.6	0.5	0.3	0.75	2.5	1.4	0.6
Parameter	l_3	l_4	l_5	l_6			
Value	0.85	1.8	7.5	2			

[1]The units of the geometric parameters are mm.

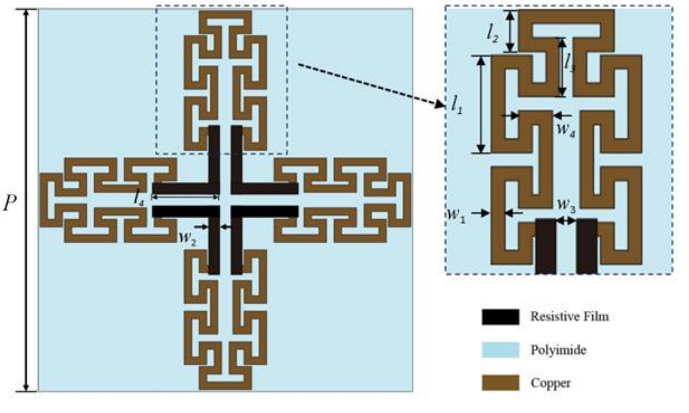

Fig. 4: Configuration and geometric parameters of the lossy impedance layer.

2.2 Analysis of the upper layer

Within the working frequency range, the top lossy layer should play the role of broadband absorber in operating range without affecting the transmission performance of the passband. The top lossy layer consists of a Jerusalem cross metal strip inserted with a resistive film (R_s=90Ω/sq), which is constructed on polyimide (ε_r=4.3, tanδ=0.0067, and thickness t_1=0.1 mm) substrate. Fig. 4 shows the detailed pattern of the lossy impedance layer.

The top layer is initially designed as an independent CAA structure, where a complete metallic sheet has been considered as the ground plane. An air spacer of 12 mm thick is present between the ground plane and the upper layer, as shown in Fig. 5(a). It can be seen from Fig. 4 that the absorbing structure is

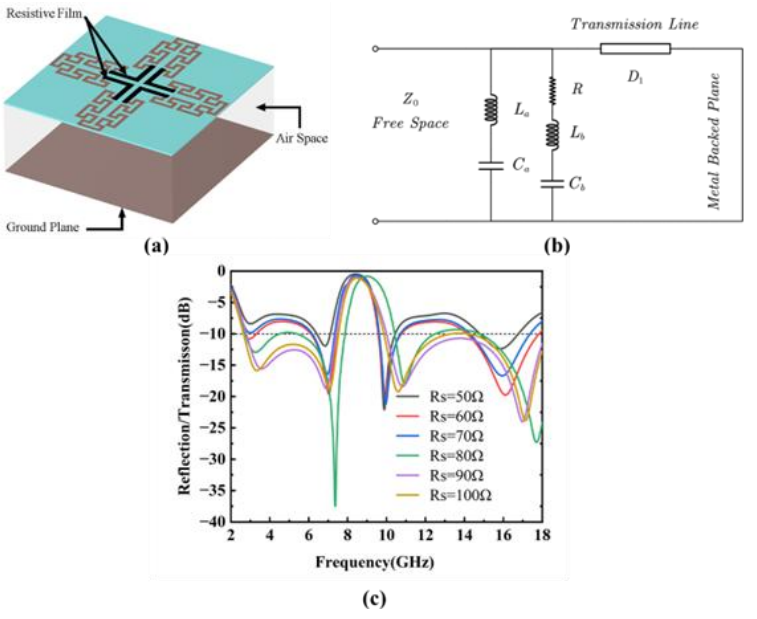

Fig. 5: (a) Resistive FSS with full ground plane. (b) Equivalent circuit of the FSS with ground plane. (c) Reflectivity for resistive films with different resistance values.

improved on the traditional square ring structure by bending the metal strip into a Jerusalem cross.

In order to improve the theoretical analysis of the design, the equivalent circuit analysis of the designed structure is specially carried out. In the EC model in Fig. 5(b), the equivalent circuit is composed of L_aC_a and RL_bC_b parallel circuits in series, where L_a and C_a are realized by bent metal loops and the gap between them, respectively. As R stands for resistive film loaded in the absorbing structure, the realization of metal strip parallel to the direction of electric field and the gap between adjacent units are equivalent to L_b and C_b respectively.

Conductor backed ground plane is represented by a short-circuited transmission line separated from the top layer by another transmission line containing a dielectric and air spacing, which is h. The working principle is quite similar to the Salisbury screen.

Fig. 5(c) illustrates the simulation performance characteristics of the standalone absorber structure with resistive films of varying resistance values, derived from numerical simulations conducted in CST Studio. Notably, the absorber achieves the optimal reflective performance at a resistance of 90 Ω. Under this condition, its reflection coefficient remains below -10 dB across two frequency bands at 2.9–6.9 GHz and 10.5–17 GHz, manifesting superior high-frequency electromagnetic wave absorption capabilities.

Since the rear side of the structure is completely laminated with a metal sheet, there is no transmission, and therefore broadband absorption is obtained for the same frequency range. At the frequencies around 5 GHz and 14GHz, Z_{FSS} gets cancelled with Z_d leading to a low valley reflectivity characteristic. So, the combination of resistive metal loop along with a full ground acts an ideal absorber.

2.3 Design and analysis of the bottom reconfigurable FSS

As shown in Fig. 6, the FSS consists of three metal layers sandwiching two Rogers RT5880 (thickness d_1=1.58 mm) substrates, the upper and lower layers of the FSS are metallic patches with the same pattern but intersecting placement directions, while there is a cross-shaped metallic grid in the middle. Two PIN diodes are respectively soldered across gaps in corresponding positions of the upper and lower metallic strip. For this second-order FSS, according to,[30] the top and bottom metal layers are capacitive while the middle layer is inductive, which satisfies the requirement of three-dimensional topology. Following the line transmission theory, we introduced the principle of the reconfigurable FSS proposed with the ideal equivalent circuit model of higher order FSS surface.

Here, high-order FSS realized using multilayer structures can produce wide transmissive bands,[31-33] and without loss of generality, an equivalent circuit model of an N-layer frequency-selective surface is given in Fig. 7(a). The FSS consists of N capacity and N-1 inductive layers, which are arranged alternately and separated by a dielectric substrate, which is equivalent to a transmission line of finite length.

An equivalent transformation method of a transmission line into a Π-type LC network consisting of an inductor L_u and two capacitors C_u was used. This method converts the FSS equivalent circuit into the form shown in Fig. 7(b), where L_u and C_u are combined with C and L generated by the metal patch and cross-

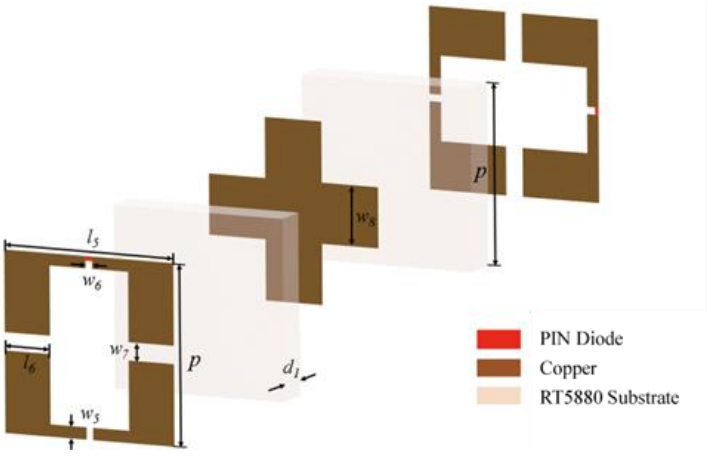

Fig. 6: Proposed design and geometric parameters of the bandpass FSS.

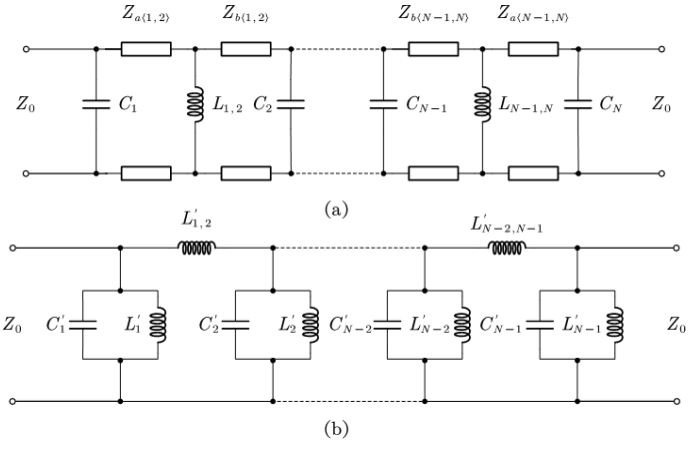

Fig. 7: ECM analysis of frequency selective surface switching schematic: (a) N-level FSS equivalent circuit model; (b) N-1 order bandpass filter equivalent circuit model.

grid to form a parallel resonator of L_n-C_n (n=1,2, 3…, N). The resonant frequency of L_n-C_n is denoted by f_n, and we define that $f_n < f_{n+1}$.The circuit model is divided into three parts, the L'_1-C'_1 and L'_{N-1}-C'_{N-1} resonators and the two-port network in the dashed box. Cascading the ABCD matrices of the three parts yields the ABCD matrix of the overall circuit as Eq. (8):

$$\begin{pmatrix} A & B \\ C & D \end{pmatrix} = \begin{pmatrix} 1 & 0 \\ \frac{1}{Z_1'} & 1 \end{pmatrix} \begin{pmatrix} A' & B' \\ C' & D' \end{pmatrix} \begin{pmatrix} 1 & 0 \\ \frac{1}{Z_{N-1}'} & 1 \end{pmatrix} \tag{8}$$

A', B', C' and D' represent the ABCD matrix elements of the two-port network in the dashed box in Fig. 7(b). As the impedance of resonators L_1-C_1 and L_{N-1}-C_{N-1}, Z_1, Z_{N-1} can be expressed as Eqs. (9) and (10):

$$Z_1' = \frac{j\omega L_1'}{1 - \omega^2 L_1' C_1'} \tag{9}$$

$$Z_{N-1}' = \frac{j\omega L_{N-1}'}{1 - \omega^2 L_{N-1}' C_{N-1}'} \tag{10}$$

The resonant frequency of these two can be written as Eqs. (11) and (12):

$$f_1' = \frac{1}{2\pi}\sqrt{\frac{1}{L_1' C_1'}} \tag{11}$$

$$f_{N-1}' = \frac{1}{2\pi}\sqrt{\frac{1}{L_{N-1}' C_{N-1}'}} \tag{12}$$

Based on the ABCD matrix, the reflection coefficient of the circuit structure in Fig. 7(b) can be written as Eqs. (13) and (14):

$$|S_{11}| = \left|\frac{A + B/Z_0 - CZ_0 - D}{A + B/Z_0 + CZ_0 + D}\right| = \left|\frac{A' + B'/Z_0 - C'Z_0 - D' + K_{1a}}{A' + B'/Z_0 + C'Z_0 + D' + K_{1b}}\right| \tag{13}$$

$$|S_{22}| = \left|\frac{-A + B/Z_0 - CZ_0 - D}{A + B/Z_0 - CZ_0 - D}\right| = \left|\frac{-A' + B'/Z_0 - C'Z_0 - D' + K_{2a}}{A' + B'/Z_0 - C'Z_0 - D' + K_{2b}}\right| \tag{14}$$

where the parameters K_{1a}, K_{2a}, K_{1b}, and K_{2b} are denoted as Eqs. (15), (16) and (17):

$$K_{1a} = \frac{B'(Z_1' - Z_{N-1}' - Z_0) - Z_0(D'Z_1' + A'Z_{N-1}')}{Z_1' Z_{N-1}'} \tag{15}$$

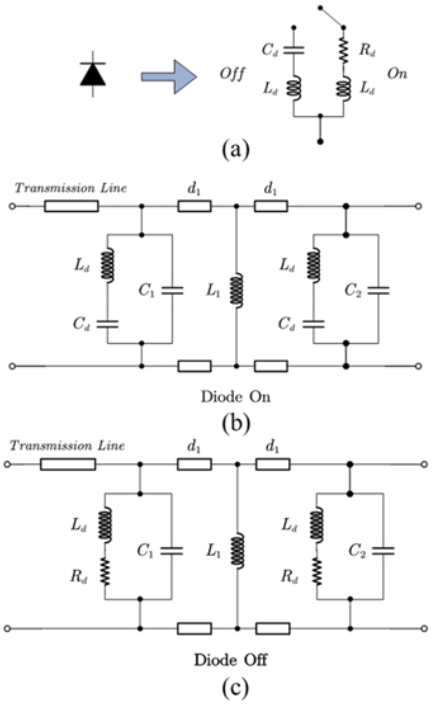

Fig. 8: Equivalent circuit representation of the bottom FSS for various biasing states of PIN diodes. (a) Equivalent circuit model of PIN diode (b) Diode ON. (c) Diode OFF.

$$K_{2a} = \frac{B'(Z_{N-1}' - Z_1' - Z_0) - Z_0(D'Z_1' + A'Z_{N-1}')}{Z_1'Z_{N-1}'} \quad (16)$$

$$K_{1b} = K_{2b} = \frac{B'(Z_1' + Z_{N-1}' + Z_0) + Z_0(D'Z_1' + A'Z_{N-1}')}{Z_1'Z_{N-1}'} \quad (17)$$

Since the impedance of a shunt resonator is infinite at its resonant frequency point and almost zero in the frequency band away from the resonant frequency point, there is $Z'_1 \approx \infty$(or $Z'_{N-1} \approx \infty$) in the frequency band around f'_1 (or f'_{N-1}) and $Z'_1 \approx 0$ (or Z'_{N-1}) in the frequency band further away from f'_1 (or f'_{N-1}). When the component parameters are left-right symmetric, there is $f'_1 = f'_{N-1}$, in which case the circuit structure shown in Fig. 7(b) is a standard N-1-order resonant coupled bandpass filter. And if $f'_1 = f'_{N-1}$.

When $f'_1 = f'_{N-1}$, in the band away from f'_1, since $Z'_1 = 0$, combining Eq. (13), Eq. (15), and Eq. (17), we can get $|S_{11}| = 1$. In the band around f'_1, since $Z'_{N-1} = 0$, combining Eq. (14), Eq. (16), and Eq. (17), we can get $|S_{22}| = 1$, which in turn shows that $|S_{12}| = 0$. From the reciprocity of passive two-port networks we can see that $|S_{21}| = |S_{12}| = 0$. Since the losses on the FSS are small, it can be deduced without considering the losses that $|S_{11}| = 1$. Therefore, $|S_{11}|$ is equal to 1 over the entire frequency band, so the circuit has reflective characteristics over the entire frequency band.

Therefore, by adjusting the capacitance value of the top (bottom) layer of the N-layer FSS, the resonant frequency of the corresponding shunt resonator can be adjusted away from the resonant frequency of the bottom (top) layer of the shunt resonator, which in turn allows the bandpass FSS to switch to the reflective plate.

Accordingly, the FSS proposed in this paper can be regarded as the same kind of model with N=3, and the PIN diode loaded is used to achieve the capacitance value adjustment of the top or bottom layer of the FSS. The equivalent circuit model of the PIN diode is shown in Fig. 8(a), which is equivalent to a series L_d-C_d when the diode is turned off, and a series L_d-R_d when the PIN diode is turned on. Table 2 shows the parameters of each component.

Table 2: The Physical Parameters of Proposed PIN Diode.

Parameter	C_d	R_d	L_d
Value	0.0245pF	7.8Ohm	0.03nH

The top and bottom layers of the FSS are two layers of metal patches loaded with diodes in the same but intersecting directions of placement, which means that this FSS is equal to loading a PIN diode on the top layer in one polarization direction and on the bottom layer in another polarization direction, thus improving polarization insensitivity. Due to the method of analyzing and loading the diode model, the equivalent circuit model of the whole underlying FSS in different states can be shown in Fig. 8(b) and. Fig. 8(c).

With the diode off, the L_d-C_d branch becomes conductive.

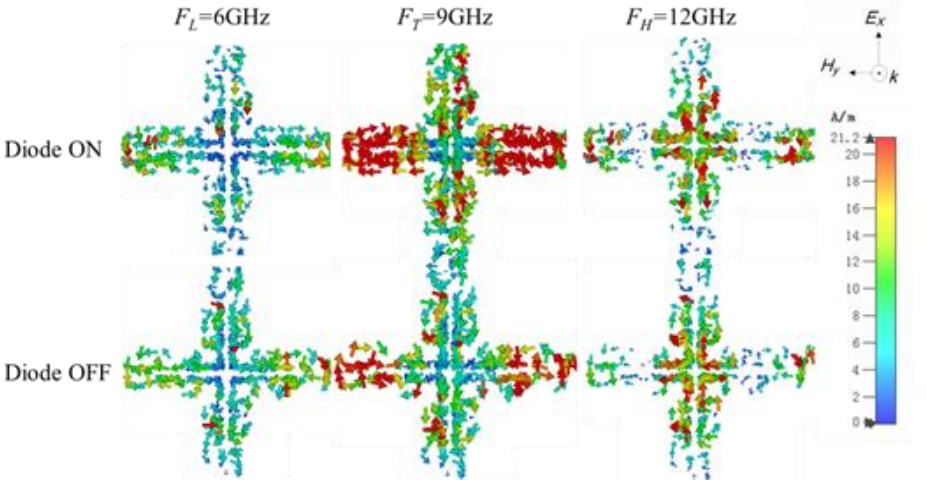

Fig. 9: Surface currents of the upper layer at lower absorption (6 GHz), upper absorption (12 GHz), and transmission bands (9 GHz).

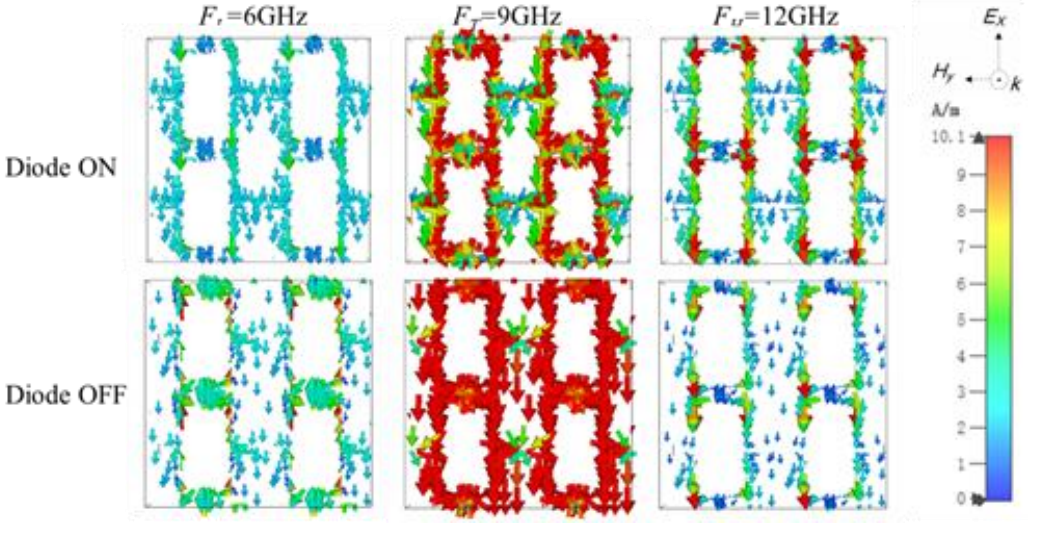

Fig. 10: Surface currents of the upper layer of the bottom FSS at lower absorption (6 GHz), upper absorption (12 GHz), and transmission bands (9 GHz).

When the diode is off, the L_d-C_d branch conducts, and since the value of L_d is very small, its effect is negligible, and capacitor C_1 is connected in parallel with the diode parasitic capacitance C_d. Because the equivalent capacitances of the top and bottom layers C_1, C_2 are both equivalent capacitances generated by the gaps between metal patches, their values are determined by the shape and size of the gaps between patches. Combined with the structure shown in Fig. 4(a), the gap shapes of the top and bottom metal patches are highly similar. Based on this, calculations using an analytical model of coupling capacitance considering the gap structure show that C_1 and C_2 are extremely close in value. From the device parameters, it is evident that the value of C_d is significantly smaller than that of C_1 and C_2. Although C_d is connected in parallel with C_1, its contribution to the total equivalent capacitance of the top layer $C_1 + C_d$ is negligible. This allows the equation $C_1+C_d \approx C_2$ to hold, ultimately ensuring that the second-order Π-type LC equivalent circuit of the FSS satisfies the symmetric bandpass condition.

When the PIN diode is turned on, the values of the parasitic inductance L_d and the on-resistance R_d are so small that the diode is similar to a short circuit that could short-circuit the capacitor C_1. The circuit shown will not resonate due to the resonant frequencies of the upper and lower layers of the FSS do not coincide with the absence of any capacitance and will then act as a perfect reflector to exhibit total reflection characteristics.

2.4 Analysis of the whole metasurface structure

To better understand the mechanism of the whole metasurface, the surface current distributions at three resonant frequencies in two states are shown in Fig. 9 and Fig. 10. We performed a surface current analysis of the upper layer, which is demonstrated in Fig. 9. It can be observed that at F_L (6 GHz)

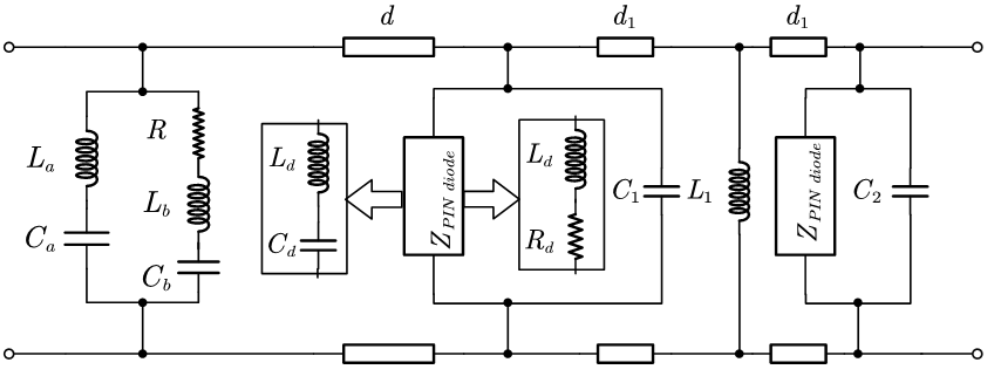

Fig. 11: Equivalent circuit representation of the proposed rasorber.

and F_H (12 GHz), the current is mainly concentrated on the square-ring patch and the resistive film, which resonates with the structure underneath and utilizes the ohmic loss mechanism of the resistive film, thus generating a good out-of-band wave-absorbing performance. At F_T (9 GHz), in the off state, currents detour around the non-conductive diode, exhibiting fragmented and weakened distributions, so the current intensity on both the metal patch and the resistive film is very small, and the electromagnetic wave is reflected back without entering the absorber because asymmetric currents partially degrade transmission efficiency. In the on state, closed-loop current circulation forms along the conductive path, concentrating near the diode and adjacent metallic elements, and the symmetric dipole-like current distribution minimizes ohmic losses, facilitating efficient wave transmission.

Since the structure has rotational symmetry and is polarization insensitive, only the case of x-polarized wave incidence is discussed. As shown in Fig. 10, when the diode is on, complementary current patterns to the upper layer are observed, enhancing interlayer coupling. There are strong resonance currencies at the edges of the metal patch and flowing through the PIN diode at both F_L (6 GHz) and F_H (12 GHz). Similarly, the surface current distribution at the F_T (9 GHz) frequency is of the same form but with a slightly weaker current strength. However, as long as the diode turns off, the underlying current path is blocked, the distribution becomes fragmented, and the coupling with the upper-layer structure is weakened. The surface currencies resonate in the rectangular structure, with little current intensity elsewhere, leading to a wide passband transmission with low insertion loss around F_T. Meanwhile, distributions remain constant at other frequency current.

At this point, through the combination of the top lossy layer and the bottom lossless FSS, we can clearly identify the metasurface structure proposed in this paper, whose equivalent circuit is shown in Fig. 11. The switching control of the PIN diode is achieved by modulating the bias voltage. When the diode in the FSS is on, the resonant frequency of the parallel resonator consisting of L_a and C_a in the impedance layer is placed outside the operating band, and the FSS is fully reflective throughout the operating band. In the off state, the change in capacitance opens the transmissive window of the FSS and the switch from reflective to transmissive is achieved.

3. Implementation and experiment

To substantiate the proposed rasorber, the prototype was fabricated by using the printed circuit board (PCB) technology. The top layer is etched on a 0.2mm-thick polyimide substrate. A sheet of resistive material with a specific resistivity of 90 Ω/sq is affixed to the top layer. The PIN diode is MADP-000907-14020 sourced from MACOM, which is a gallium aluminum arsenide PIN diode and achieves switching states as shown in Fig. 8(a). These diodes are integrated into the bottom FSS, utilizing surface-mount technology. To establish an 8mm airspace between the top and bottom FSS strata, PCB spacers are positioned at the sample's corners. The lower FSS incorporates two layers of Rogers RT5880, each measuring 1.575mm(d_1) in thickness. A photograph of the fabricated metasurface prototype with the size of 280 × 280 mm is shown in Fig. 12 and it comprises a total of discrete resistors and 2738 PIN diodes, both of which are soldered into the assembly.

Here we have performed simulations and measurements to verify the feasibility of producing structure at different angles and with different polarized incident waves. In order to obtain accurate experimental results, the structure was measured in an anechoic chamber with the prototype mounted on a stand and identical standard gain horn antennas connected to a vector network analyzer. The horn antennas were used to transmit and receive signals from the vector network analyzer. The angle and distance between the horn antennas and the prototype were varied by changing the position of the horn antennas to measure different s-parameters.

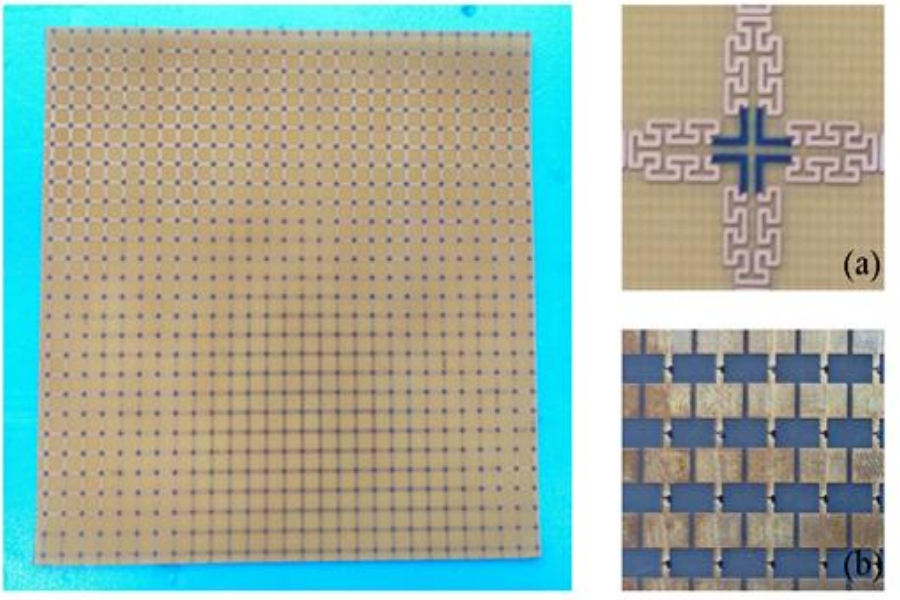

Fig. 12: Fabricated prototype of the rasorber. (a) Top lossy layer. (b) Bottom lossless FSS.

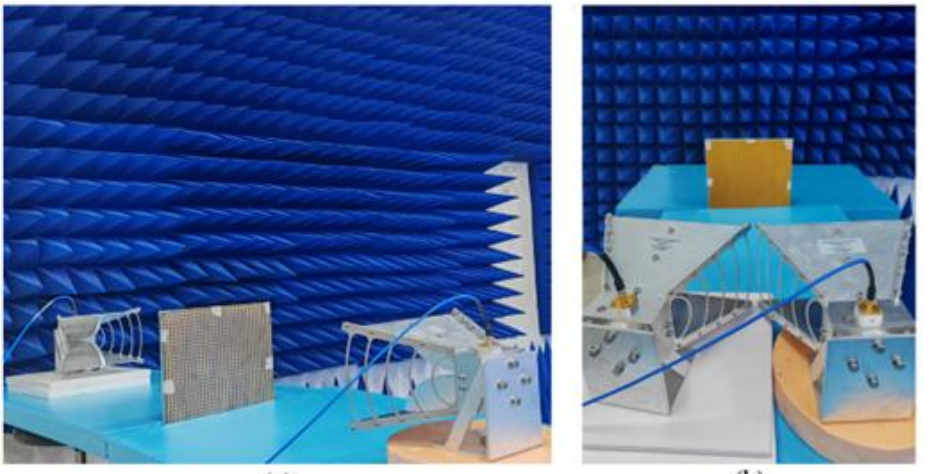

Fig. 13: Measurement setup of (a) Transmission and (b) Reflection.

The prototype was placed in the center of the absorbing screen and its center carefully aligned with its center of the antenna hole. The measurement setups for transmission and reflection are shown in Fig. 13(a) and (b). For reflection measurements, the antenna is orientated differently at different angles of incidence, respectively. In addition, for transmittance measurements, the absorbing screen with the sample was rotated to oblique incidence and the transmittance of the absorbing screen without the sample was normalized.

As specifically shown in Fig. 12(b) (the bottom lossless FSS layer), the PIN diodes were soldered across the pre-designed gaps of the FSS metallic patches. Notably, the continuous copper patterns of the FSS served as the integrated bias circuit for the diodes, this design avoids extra wiring that might interfere with electromagnetic performance. A DC power supply was connected to the edge of the FSS metallic patterns to deliver bias voltage: +5 V DC was applied to turn the diodes ON (enabling the conductive path for the transmission window), and 0 V DC was used to turn them OFF (blocking the path to achieve reflective stealth mode). The bias voltage was stable throughout measurements to ensure consistent switching between the two states.

When in the transmissive state (PIN diodes OFF), the prototype provides broadband transmission with a transmission window of less than 2 dB insertion loss in the 7.5-9.8 GHz range (as shown in Fig. 14 (a) and (b)), which verifies the bandpass mechanism deduced from the equivalent circuit model. This state corresponds to the FSS forming a matched LC resonant path, just as the ECM predicts for diode-OFF conditions. Meanwhile, the proposed structure achieves over 90% absorption at 3.4-6.2 GHz and 9.1-15.2 GHz, consistent with the ECM's description of the upper lossy

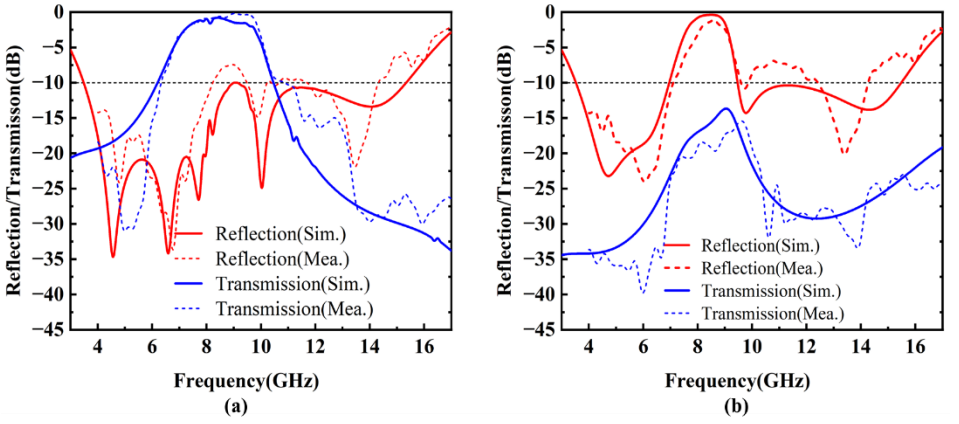

Fig. 14: Simulated and measured performance of the metasurface under linearly normal incident waves. (a) and (b) are simulated and measured results of transmission mode and absorption mode.

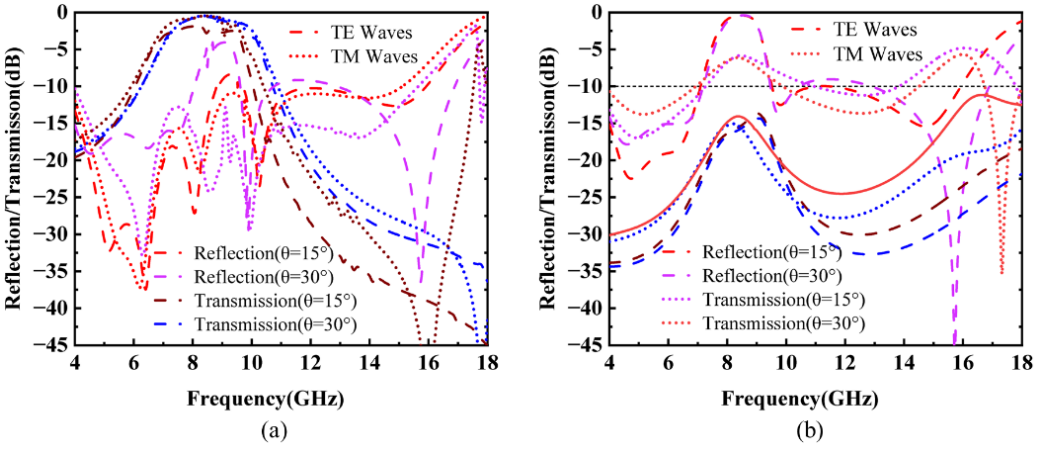

Fig. 15: Measured performance of the metasurface under linearly oblique incident waves. (a) PIN OFF, (b) PIN ON.

Table 3: Comparison between Our Work and Previous Efforts.

Ref.	EM Response	Maximum transmission and fT	Lower Absorption band	Upper Absorption band	Polarization	Transmission swichable
[7]	T-A	0.82 GHz/0.5dB	-	4-8 GHz	Dual	No
[14]	A-T-A	8.5 GHz /2 dB	4.1-7.8 GHz	9.3-13.8 GHz	Dual	No
[18]	A-T	10.15 GHz /0.6 dB	3.8-8.6 GHz	-	Single	Yes
[31]	A-T-A	4.17 GHz /1 dB	1-4.39GHz	6.04-7.71 GHz	Dual	Yes
[33]	A-T-A	4.15GHz /1 dB	0.85-2.93 GHz	5.4-7.47 GHz	Single	Yes
This work	A-T-A	8.4 GHz /0.78 dB	3.4-6.2 GHz	9.1-15.2 GHz	Dual	Yes

layer's absorption function. In the reflective state (PIN diodes ON), the operating band converts from transmission to all-reflective characteristics, and broadband absorption is realized at 3.5-6.9 GHz and 9.5-15.4 GHz, which matches the ECM's conclusion that diode conduction causes impedance mismatch in the FSS, switching it to total reflection while maintaining the lossy layer's absorption. The simulation results are in good agreement with the measured results; tiny differences mainly stem from the gap between the far-field model, actual far-field measurements, and assembly tolerances.

In addition, the prototype has good angular stability in the range of 15 ~ 30° of the incidence angles, as shown in Fig. 15. The solid and dashed lines in the figure show the performance of the unit under oblique TE-polarized incident waves and tm-polarized incident waves, respectively. Please note that the current anechoic chamber test platform supports incident

angles of up to 60°. However, beyond 30°, measurement repeatability and stability are significantly compromised due to increased electromagnetic leakage from the test fixture and stronger mutual coupling among the metasurface unit cells at large oblique angles. This introduces non-negligible measurement uncertainties. Therefore, data acquired beyond 30° is not considered reliably reproducible.

The results show that under 30° oblique incidence, the deviation between the simulated and measured values of the unit cell's reflection coefficient (S_{11}) is less than 1.5 dB, and the deviation of the transmission coefficient (S_{21}) is controlled within 1 dB. The frequency offset of the core transmission window is only 0.2 GHz, and the dual absorption bands remain stable without obvious offset. This stability stems from the symmetry of the Jerusalem cross structure in the unit cell, which can effectively suppress electromagnetic response fluctuations caused by 30° oblique incidence.

Table 3 compares our work with previous works. Compared with the reference group, this work demonstrates distinct advantages. Its total absorption bandwidth is wider than those reported in recent studies within the group, while its insertion loss is lower than that of most works in the same reference group. In addition, it retains dual-polarization insensitivity while achieving superior overall performance. The proposed one has flexible realization of function switching of the operating range, and has efficient transmission and broadband absorption, far beyond that of other existing reconfigurable counterparts, presenting promising engineering application prospects.

4. Conclusion

In this paper, numerical simulation and experimental demonstration of a reconfigurable metasurface are presented. The most promising feature of the structure is its unique ability to offer switchable transmission or reflection (T/R) band between two broadband absorptions. The transmission line theory is used to analyze its working principle by establishing an equivalent circuit model. The lossless FSS has been carefully designed to enable switching between being a transmissive window and an all-reflective substrate. Simulation results based on this design manifest a transmission band of 7.5-9.8 GHz with insertion loss less than 2 dB which could switch to perfect reflection. The reflectivity remains below -10 dB in the 3.4-6.2 GHz and 9.1-15.2 GHz bands. We fabricated an experimental prototype and verified the feasibility of the method under full-wave measurements.

The experimental results show that the simulation results are in great agreement with the experimental results. It is hoped that the proposed design will find its use in reducing RCS, airborne, stealth applications, and various active FSS designs.

Acknowledgments

This work was supported in part by the National Key Research and Development Program of China under Grant SQ2022YFB3806200, the National Natural Science Foundation of China under Grant No. 52272101, the Natural Science Foundation of Shaanxi Province under Grant Nos. 2024JC-YBMS-462, 2024JC-YBMS-518, 2024JC-YBON-0721, and the Postdoctoral Science Foundation of China under Grant No. 2019M651644. We also thank Air Force Engineering University and Shaanxi Key Laboratory of Artificially-Structured Functional Materials and Devices for providing the testing platform support.

Conflict of Interest

All authors declare that there are no commercial interests, personal relationships, or other conflicts of interest that may affect the objectivity of this research during the research and publication of this paper.

Supporting Information

Not applicable.

CRedit Statement

Hao Yang: Conceptualization, Methodology, Investigation, Data curation, Formal analysis, Writing - Original draft, Validation (First author, Responsible for the core research and writing of the full paper), **Yongfeng Li:** Supervision, Writing - Review & editing, Funding acquisition, Direction (Corresponding author, Responsible for project coordination and paper review), **Lixin Jiang:** Investigation, Formal analysis (Assisted), **Zhe Qin:** Investigation, Resources (Literature collection), **Lei Wang:** Validation (Simulation), Data curation (Data recording), **Jiechu Liu:** Investigation (Sample preparation), Validation (Assisted), **Zhihao Guo:** Resources (Literature research), Writing - editing (Format checking), **Lin Zheng:** Data curation (Data visualization), Resources (Equipment support); **Hongya Chen:** Validation (Experimental repetition), Data curation (Data verification), **Wenjie Wang:** Supervision, Writing - Review & editing, Communication (Corresponding author, Responsible for project supervision and final paper review), **Jiafu Wang:** Resources (Technical support), Discussion (Result discussion).

References

[1] E. Pelton, B. Munk, A streamlined metallic radome, *IEEE Transactions on Antennas and Propagation*, 1974, **22**, 799-803, doi: 10.1109/TAP.1974.1140896.

[2] T. K. Wu, Frequency Selective Surface and Grid Array,

Technology & Engineering, Wiley, 1995, **40**, 331, ISBN-0471311898.

[3] B. A. Munk, Frequency selective surfaces: theory and design, *Engineering Physics*, 2000, doi:10.1002/0471723770.

[4] L. Jiang, Y. Li, H. Yang, M. Yan, J. Jiang, Y. Zhang, Z. Qin, W. Yang, H. Chen, Y. Pang, Z. Guo, L. Zheng, J. Wang, S. Qu, Beam scanning with ultra-low sidelobes and in-band ultra-low scattering characteristics empowered by single space-time-coding radiation-scattering metasurface, *Advanced Science*, 2025, **12**, e2413429, doi: 10.1002/advs.202413429.

[5] B. A. Munk, Metamaterials: Critique and Alternatives, Hoboken, NJ, *General & Introductory Materials Science*, Wiley, 2009, 189, ISBN: 978-0-470-37704-8.

[6] F. Costa, A. Monorchio, A frequency selective radome with wideband absorbing properties, *IEEE Transactions on Antennas and Propagation*, 2012, **60**, 2740-2747, doi: 10.1109/TAP.2012.2194640.

[7] Q. Chen, J. Bai, L. Chen, Y. Fu, A miniaturized absorptive frequency selective surface, *IEEE Antennas and Wireless Propagation Letters*, 2014, **14**, 80-83, doi: 10.1109/LAWP.2014.2355252.

[8] H. Tu, P. Liu, J. Huang, Y. Qin, A miniaturized frequency selective rasorber with tunable passband, *International Symposium on Electromagnetic Compatibility - EMC EUROPE*, Angers, France, September 4-7, 2017, 1-4, doi: 10.1109/EMCEurope.2017.8094797.

[9] Q. Chen, D. Sang, M. Guo, Y. Fu, Frequency-selective rasorber with interabsorption band transparent window and interdigital resonator, *IEEE Transactions on Antennas and Propagation*, 2018, **66**, 4105-4114, doi: 10.1109/TAP.2018.2835671.

[10] A. A. Omar, Z. Shen, H. Huang, Absorptive frequency-selective reflection and transmission structures, *IEEE Transactions on Antennas and Propagation*, 2017, **65**, 6173-6178, doi: 10.1109/TAP.2017.2754463.

[11] K. Zhang, W. Jiang, S. Gong, Design bandpass frequency selective surface absorber using LC resonators, *IEEE Antennas and Wireless Propagation Letters*, 2017, **16**, 2586-2589, doi: 10.1109/LAWP.2017.2734918.

[12] D. Lim, S. Lim, Ultrawideband electromagnetic absorber using sandwiched broadband metasurfaces, *IEEE Antennas and Wireless Propagation Letters*, 2019, **18**, 1887-1891, doi: 10.1109/LAWP.2019.2932399.

[13] J. Li, A. Jana, Y. Yuan, K. Zhang, S. N. Burokur, P. Genevet, Exploiting hidden singularity on the surface of the Poincaré sphere, *Nature Communications*, 2025, **16**, 5953, doi: 10.1038/s41467-025-60956-2.

[14] B. Bandyopadhyay, A. K. Shahi, A. Dileep, M. Saikia, K. V. Srivastava, Polarization insensitive broadband frequency selective rasorber with improved selectivity for stealth applications, *18th European Conference on Antennas and Propagation (EuCAP)*, Glasgow, United Kingdom, March 17-22, 2024, 1-5.

[15] X. Pang, S. Mao, S. Sun, B. Wu, Lowpass frequency selective rasorber with wideband absorption using multilayer graphene-based metasurface, *International Conference on Microwave and Millimeter Wave Technology (ICMMT)*, Harbin, China, August 12-15, 2022, 1-3, doi: 10.1109/ICMMT55580.2022.10022672.

[16] J. Li, Y. Yuan, G. Yang, Q. Wu, W. Zhang, S. N. Burokur, K. Zhang, Hybrid dispersion engineering based on chiral metamirror, *Laser & Photonics Reviews*, 2023, **17**, 2200777, doi: 10.1002/lpor.202200777.

[17] L. Jiang, Y. Li, H. Yang, L. Zheng, H. Chen, W. Wang, Z. Qin, M. Yan, J. Jiang, Z. Zhu, Y. Meng, J. Wang, S. Qu, Smart jamming cloak for moving targets with full polarization response, *IEEE Transactions on Microwave Theory and Techniques*, 2025, **73**, 703-713, doi: 10.1109/tmtt.2024.3423007.

[18] Q. Zhou, H. Zhou, L. Huang, Z. Wu, Z. Zhang, A reconfigurable frequency selective rasorber with switchable transmission/reflection/absorption band, *IEEE Transactions on Electromagnetic Compatibility*, 2024, **66**, 1371-1381, doi: 10.1109/TEMC.2024.3422830.

[19] Y. Yu, Z. Shen, T. Deng, G. Luo, 3-D frequency-selective rasorber with wide upper absorption band, *IEEE Transactions on Antennas and Propagation*, 2017, **65**, 4363-4367, doi: 10.1109/TAP.2017.2712812.

[20] L. Jiang, Q. Yuan, H. Yang, Y. Li, L. Zheng, Z. Zhu, S. Liang, Y. Pang, H. Wang, J. Wang, S. Qu, Shape memory alloy-based 3D morphologically reconfigurable chiral metamaterial for tailoring circular dichroism by voltage control, *Photonics Research*, 2023, **11**, 373, doi: 10.1364/prj.480979.

[21] J. Huang, L. Yuan, J. Liao, Y. Liu, D. Li, Y. Wang, H. Lin, C. Ji, X. Ma, C. Huang, X. Luo, A Janus spectrally selective glazing toward all-season energy-efficient windows, *Small*, 2025, **21**, e2407204, doi: 10.1002/smll.202407204.

[22] H.-X. Xu, G. Hu, Y. Wang, C. Wang, M. Wang, S. Wang, Y. Huang, P. Genevet, W. Huang, C.-W. Qiu, Polarization-insensitive 3D conformal-skin metasurface cloak, *Light: Science & Applications*, 2021, **10**, 75, doi: 10.1038/s41377-021-00507-8.

[23] R. You, W. Geng, Q. Guo, A multifunction frequency-selective rasorber with multiple transmission and absorption bands, *IEEE 11th Asia-Pacific Conference on Antennas and Propagation (APCAP)*, Guangzhou, China, November 22-24, 2023, 1-2, doi: 10.1109/APCAP59480.2023.10470035.

[24] L. Xiong, P. Chai, A. Fu, Y. Fu, R. Tan, P. Chen, Design of a multifunctional metasurface with frequency-selective absorbing properties, *IEEE International Workshop on Electromagnetics:*

Applications and Student Innovation Competition (iWEM), Harbin, China, July 15-18, 2023, 130-132, doi: 10.1109/iWEM58222.2023.10234882.

[25] R. Zhu, J. Wang, T. Qiu, D. Yang, B. Feng, Z. Chu, T. Liu, Y. Han, H. Chen, S. Qu, Direct field-to-pattern monolithic design of holographic metasurface *via* residual encoder-decoder convolutional neural network, *Opto-Electronic Advances*, 2023, **6**, 220148, doi: 10.29026/oea.2023.220148.

[26] Z. Chu, X. Cai, R. Zhu, T. Liu, H. Sun, T. Li, Y. Jia, Y. Han, S. Qu, J. Wang, S. L. S. China, Complete-basis-reprogrammable coding metasurface for generating dynamically-controlled holograms under arbitrary polarization states, *Opto-Electronic Advances*, 2024, **7**, 240045, doi: 10.29026/oea.2024.240045.

[27] Z. Wu, Q. Zhou, P. Liu, M. Lin, Active frequency selective rasorber with switchable transmission band and tunable absorption band, *IEEE Microwave and Wireless Technology Letters*, 2023, **33**, 1247-1250, doi: 10.1109/LMWT.2023.3277069.

[28] D. M. Pozar, Microwave Engineering, 4th ed. Hoboken, *Microwave Theory & Techniques*, Wiley, 2011, 752, ISBN: 978-0-470-63155-3.

[29] L. Wu, S. Zhong, J. Huang, T. Liu, Broadband frequency-selective rasorber with varactor-tunable interabsorption band transmission window, *IEEE Transactions on Antennas and Propagation*, 2019, **67**, 6039-6050, doi: 10.1109/TAP.2019.2916739.

[30] M. A. Al-Joumayly, N. Behdad, A generalized method for synthesizing low-profile, band-pass frequency selective surfaces with non-resonant constituting elements, *IEEE Transactions on Antennas and Propagation*, 2010, **58**, 4033-4041, doi: 10.1109/TAP.2010.2078474.

[31] H. Jiang, Q. Hu, Q. Xue, Reconfigurable rasorber with elliptic filtering response, *IEEE MTT-S International Wireless Symposium (IWS)*, Beijing, China, May 16-19, 2024, 1-3, doi: 10.1109/IWS61525.2024.10713786.

[32] M. Guo, D. Sang, F. Yuan, T. Guo, Y. Zheng, Q. Chen, Y. Fu, Broadband absorptive frequency-selective rasorber based on multilayer resistive sheets using multilayer resonator, *IEEE Transactions on Antennas and Propagation*, 2022, **70**, 2009-2022, doi: 10.1109/TAP.2021.3111215.

[33] R. Li, J. Tian, B. Jiang, Z. Lin, B. Chen, H. Hu, A switchable frequency selective rasorber with wide passband, *IEEE Antennas and Wireless Propagation Letters*, 2021, **20**, 1567-1571, doi: 10.1109/LAWP.2021.3091480.